

Accurate Kohn-Sham auxiliary system from the ground state density of solids

Ayoub Aouina,^{1,2} Matteo Gatti,^{1,2,3} Siyuan Chen,⁴ Shiwei Zhang,^{5,4} and Lucia Reining^{1,2}

¹*LSI, CNRS, CEA/DRF/IRAMIS, École Polytechnique, Institut Polytechnique de Paris, F-91120 Palaiseau, France*

²*European Theoretical Spectroscopy Facility (ETSF)*

³*Synchrotron SOLEIL, L'Orme des Merisiers, Saint-Aubin, BP 48, F-91192 Gif-sur-Yvette, France*

⁴*Department of Physics, College of William & Mary, Williamsburg, Virginia 23185, USA*

⁵*Center for Computational Quantum Physics, Flatiron Institute, New York, New York 10010, USA*

(Dated: July 11, 2022)

The Kohn-Sham (KS) system is an auxiliary system whose effective potential is unknown in most cases. It is in principle determined by the ground state density, and it has been found numerically for some low-dimensional systems by inverting the KS equations starting from a given accurate density. For solids, only approximate results are available. In this work, we determine accurate exchange correlation (xc) potentials for Si and NaCl using the ground state densities obtained from Auxiliary Field Quantum Monte Carlo calculations. We show that these xc potentials can be rationalized as an ensemble of environment-adapted functions of the local density. The KS band structure can be obtained with high accuracy. The true KS band gap turns out to be larger than the prediction of the local density approximation, but significantly smaller than the measurable photoemission gap, which confirms previous estimates. Finally, our findings show that the conjecture that very different xc potentials can lead to very similar densities and other KS observables is true also in solids, which questions the meaning of details of the potentials and, at the same time, confirms the stability of the KS system.

I. INTRODUCTION

Density Functional Theory^{1,2} (DFT) is undoubtedly one of the biggest success stories of condensed matter theory, since it has made realistic electronic structure calculations possible for a huge range of materials, and since it has led to numerous insights^{3,4}. Two main problems had to be overcome in order to make DFT applicable in practice: first, it was necessary to find reliable approximations for the total energy as functional of the ground state density; second, an efficient way to determine the ground state density itself was needed. The solution to both problems relies on the approach of Kohn and Sham², where the interacting system is mapped onto an auxiliary system of non-interacting electrons with an effective Kohn-Sham (KS) potential that is designed to yield the ground state density. The exchange-correlation (xc) contribution to this potential, $v_{xc}(\mathbf{r})$, and to the xc energy density per particle, $\epsilon_{xc}(\mathbf{r})$, is unknown in most systems. The initial breakthrough came with the Local Density Approximation² (LDA). This approximation takes the energy density, and hence $v_{xc}(\mathbf{r})$, locally from the homogeneous electron gas (HEG), where it was calculated using Quantum Monte Carlo⁵ (QMC). However, to find approximations that are systematically better than the LDA has turned out to be exceedingly difficult^{6,7}. Today, in spite of the developments of successful gradient corrections and sophisticated approximations tailored by exact constraints^{8–11}, one may say that there is still no generally established multi-purpose approximation beyond the LDA. One of the difficulties is that it is not easy to benchmark v_{xc} . First, the Kohn-Sham potential is not an observable by itself, which means, there are no experimental data to compare with. Second, since v_{xc} is the potential of an *auxiliary* system, besides the density,

any other observables calculated in the KS system can in principle be arbitrarily far from measured values. The prototype example for this dilemma is the KS eigenvalue band gap^{12–14}. For example in the LDA, this KS gap is in general much smaller than the fundamental gap extracted from direct and inverse photoemission^{15,16}. Since there is no reason for the gap of the auxiliary KS system to equal the photoemission gap of the true material^{2,17}, the respective errors of the LDA and of the KS system itself have been a matter of debate for many years. Results derived from many-body perturbation theory to first order in the screened Coulomb interaction^{18–26} gave evidence that the error in simple semiconductors is mainly due to the auxiliary nature of the KS system, reflected as a missing contribution that stems from a derivative discontinuity^{12–14}, rather than due to the LDA. However, these are merely estimates based on perturbation theory, and the numerically exact KS potential and KS band gap of solids remain to date unknown.

More information is available in low-dimensional, often finite, systems, where ways have been proposed to invert the KS equations and find the KS potential starting from a given density^{27–30}. This density could be determined by analytical or numerical methods. This has given precious insight about the potential and observables in the KS system^{31–46}. For example, in the helium atom the exact HOMO lies about 25 eV below the vacuum level, and an additional electron is unbound. The exact KS HOMO-LUMO gap, instead, turns out to be only 20.3 eV, since KS binds the LUMO^{36,47,48}. On top of this underestimate, the LDA reduces the HOMO-LUMO gap further, yielding 15.85 eV. The inversion of the KS system is not an easy task, though, and in particular a finite basis set may lead to drastically modified results^{49–53}. Moreover, small changes in the density can yield large differences

in the potential^{54,55}. Altogether, a reliable inversion of the KS equations remains a difficult task even for finite systems, and while various methods have been proposed to overcome the problems, research in this direction is still ongoing^{54–65}.

In realistic three-dimensional periodic systems, to the best of our knowledge, no results for v_{xc} obtained directly from a numerically exact density are available. This has several reasons, including the fact that data for numerically exact densities of solids were not available in the literature, and that the inversion in extended three-dimensional systems may bear new technical difficulties. Therefore, to date a series of important fundamental questions remain to be answered, in particular: *Can one invert in practice the KS equations in an extended three-dimensional system and if yes, how, and which kind of precision can be obtained? How different is the resulting v_{xc} from standard approximations for solids, such as the LDA or Perdew-Burke-Ernzerhof (PBE) generalised gradient approximation⁹ (GGA)? What about observables in this numerically exact KS system, and in particular, the band gap? How much does v_{xc} depend on details of the density? And if it depends significantly, do the resulting changes have an impact on other KS observables?* Starting from nearly numerical exact densities⁶⁶ for the simple semiconductor bulk silicon and insulating sodium chloride obtained by the Auxiliary Field (AF) QMC method^{67,68} in Ref.⁶⁹, in the present work we answer these long-standing questions.

II. HOW TO INVERT THE KS PROBLEM IN INFINITE SYSTEMS

The probably simplest algorithm to obtain the KS potential from a given density n_{ref} has been proposed for finite systems by van Leeuwen and Baerends²⁷. In its original form it was derived by solving the KS equations for the KS potential v_{KS} . The result was then translated into an iteration procedure which relates a potential v^{i+1} at step $i+1$ to the potential v^i at step i by the ratio of the target density n_{ref} and the density n^i at step i . As pointed out in³⁰, the best use of this ratio depends on the sign of the potential that is updated: for example, v may be either the usually negative total v_{KS} , or its rather positive interaction part $v_H + v_{\text{xc}}$ with v_H the Hartree potential. In the present work we use

$$v_{\text{xc}}^{i+1}(\mathbf{r}) = \frac{n_{\text{ref}}(\mathbf{r}) + a}{\tilde{n}^i(\mathbf{r}) + a} v_{\text{xc}}^i(\mathbf{r}), \quad (1)$$

where a is a parameter that avoids instabilities in regions of very low density as suggested in²⁷, and the mixing $\tilde{n}^i = \alpha n^{i-1} + (1-\alpha)n^i$, with $0 < \alpha < 1$, is introduced to smooth the convergence. This density \tilde{n}^i is also used to update the Hartree potential at each iteration. Eq. (1) is clearly a good strategy if v_{xc} is negative, and if the density at a point \mathbf{r} is determined only by the KS potential at that same point. Suppose that at a given iteration

$\tilde{n}^i(\mathbf{r})$ is larger than $n_{\text{ref}}(\mathbf{r})$. The algorithm then decreases the absolute value of $v_{\text{xc}}(\mathbf{r})$. If the exchange-correlation potential is negative, this step makes the potential more shallow, and less density will be attracted to the point \mathbf{r} in the next iteration, which pushes the solution in the good direction. Of course, it is not true that $n(\mathbf{r})$ depends only on the KS potential in the same point \mathbf{r} , and it has to be seen to which extent the relation is near-sighted enough to make the algorithm work in a solid.

The negative sign of the potential that is updated in (1) is crucial for the algorithm to work, because a positive sign would drive the result in the wrong direction. However, contrary to the HEG, a real system can also exhibit regions of positive v_{xc} . Moreover, while in a low-dimensional system one can impose that the potential tends to zero at large distances, in a three-dimensional solid the zero of the potential is not defined. This fact represents both an advantage and a drawback. On the upside, it allows us to introduce a rigid negative shift such that the potential remains negative throughout the iteration. This shift is arbitrary within reasonable limits: if it is too small, positive regions may appear and become an obstacle for convergence. If it is too large, the algorithm becomes unstable, as the shift is multiplied at every step by the density ratio. Reasonable values lie within the maximum amplitude of the potential. On the downside, iteration of (1) yields v_{xc} only up to a constant. This is not due to our introduction of a shift, but to the fact that the density does not contain information about the absolute value of the potential¹. Therefore, this limitation cannot be avoided. The resulting potential can, however, be used to calculate a well defined density and KS observables such as the KS band structure (besides the meaningless constant shift).

We have tested the algorithm using the LDA, and we have found it to be sufficiently accurate to support all our claims below. Detailed results of the tests can be found in Appendix B. App. C shows that the final results do not depend on the starting point of the iterative procedure, including starting points as far from the final result as, e.g., $0.1 \times v_{\text{xc}}^{\text{LDA}}$. For the results shown in the following, we use as starting point $0.3 \times v_{\text{xc}}^{\text{LDA}}$ with a rigid downwards shift of 0.2 Hartree for silicon and 0.4 Hartree for NaCl. In the following, we report results in atomic units for both densities (expressed in bohr^{-3}) and xc potentials (in Hartree).

III. RESULTS

A. Kohn-Sham potential of silicon and sodium chloride

We have applied the algorithm to obtain the exchange-correlation potential from the charge density obtained by AFQMC calculations. For silicon, we have used the results of Ref.⁶⁹. For NaCl, we have applied additional symmetry operations to the density from the same

Ref.⁶⁹. Since the QMC data is noisy, the inversion has a more limited precision than in the case of, e.g., clean LDA data (see App. D). The Mean Absolute value of the Percentage Error (MeAPE) of the density of silicon does not fall below 0.02%, while the Maximum (over the unit cell) of the Absolute value of the Percentage Error (MaAPE) of the density decreases to 0.38% at $i = 20$ iterations. This is in any case sufficient to make significant distinctions between different densities and potentials. The upper panel of Fig. 1 shows the Local Percentage Difference (LPD) of the iterative density with respect to the QMC density after 20 iterations (blue line), $100 \times (1 - n^{\text{QMC},20}(\mathbf{r})/n_{\text{QMC}}(\mathbf{r}))$, along a path through the unit cell (the same as in Ref.⁶⁹, see the inset to the second panel of Fig. 1). The result stays well within the stochastic error bar of the QMC calculation (grey area). For comparison, we also show the LPD of the LDA and PBE densities (dot-dashed orange and dashed green lines, respectively), with respect to the QMC. As also shown in Ref.⁶⁹, differences between LDA, PBE and the QMC densities are largest on the atoms and also in other regions of low density⁷⁰ (see the magenta line in the second panel of Fig. 1), but they are still significant in regions of higher density, along the (110) direction, where LDA and PBE are very similar, but differ from the QMC result. Most importantly, the differences between different densities are much larger than the error due to the inversion of the QMC density: while the MeAPE at $i = 20$ is 0.04%, the mean absolute relative difference between the LDA and QMC densities is 1.93 %, and it is 1.07 % between the PBE and QMC densities.

The xc potentials are compared in the third panel of Fig. 1. For this comparison, the potentials are aligned at their average value. Our numerically determined and supposedly most accurate KS xc potential, obtained from the QMC density, is similar to the local and semi-local approximations. This result is stable: the QMC result obtained at $i = 10$, where the MaAPE and MeAPE on the density are 0.90 % and 0.09 %, respectively, is almost indistinguishable from the one at $i = 20$. The differences between QMC on one side, and LDA and PBE on the other side, can be appreciated in the bottom panel, which shows the LPD of LDA and PBE with respect to the QMC xc potential obtained at $i = 20$. These differences are similar for LDA and PBE along most of the path. The MeAPE with respect to the QMC result for potentials is 3.90 % for the LDA and 3.88 % for the PBE: of similar order, though larger, than the MeAPE of the densities. Instead, the LPD of the QMC potential at $i = 10$ with respect to the potential obtained at $i = 20$ can hardly be seen. We have hence reached sufficient precision on the density, which lies within the QMC error bar, and the xc potential, which shows some differences with respect to common functionals. The effect of iterating further using the noisy QMC data is discussed in the App. D.

Results for sodium chloride show similar trends, with even better convergence properties of the potential due to the fact that our QMC density for NaCl is less noisy than

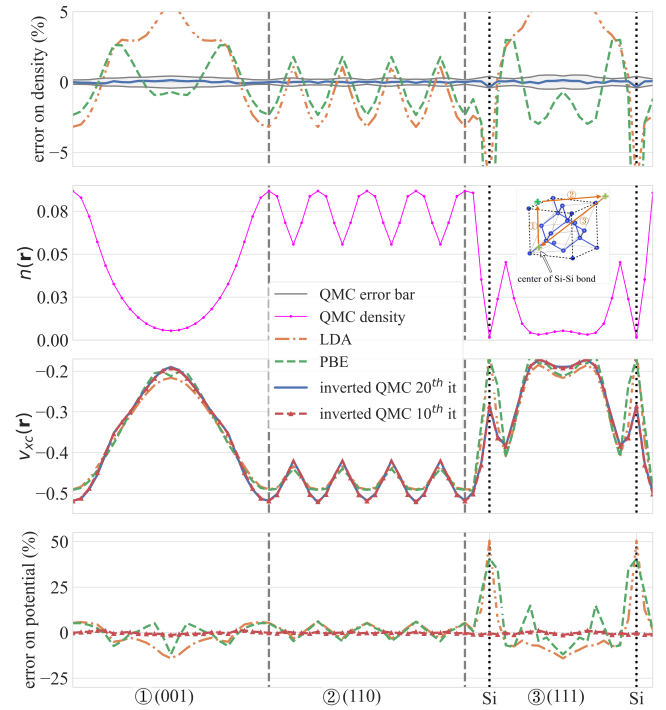


FIG. 1. Density and xc potential of bulk silicon along the same path across the unit cell as in Ref.⁶⁹. The positions of atoms are indicated by dotted vertical lines. The iterative inversion follows Eq. (1) with the QMC density n_{QMC} of silicon as reference density. The potential $v_{\text{xc}}^{\text{QMC},20}$ is obtained after $i = 20$ iterations. The density $n_{\text{QMC},20}$ is calculated using $v_{\text{xc}}^{\text{QMC},20}$ in the KS equation. The MaAPE at $i = 20$ compared to n_{QMC} is 0.38 %, and the MeAPE is 0.04%. Top panel: LPD of $n_{\text{QMC},20}$ (blue), self-consistent LDA n_{LDA} (orange), and PBE n_{PBE} (green) densities with respect to n_{QMC} . The grey area is the stochastic error bar of the QMC density. Second panel: The QMC density n_{QMC} (magenta line). The inset shows the chosen path across the crystal from Ref.⁶⁹. Third panel: $v_{\text{xc}}^{\text{QMC},20}$ (blue), $v_{\text{xc}}^{\text{LDA}}$ (orange), $v_{\text{xc}}^{\text{PBE}}$ (green), and $v_{\text{xc}}^{\text{QMC},10}$ (red). Note that the two QMC potentials (blue and red lines) are almost indistinguishable. The average potentials are aligned. Bottom panel: LPD of xc potentials with respect to $v_{\text{xc}}^{\text{QMC},20}$ for LDA (orange), PBE (green), and QMC at $i = 10$ (red).

the one of silicon in the important regions of high density (see also App. D 3). For the density, we obtain a MeAPE of 0.03% and a MaAPE of 0.29% at $i = 200$. Here, analogous to Fig. 1 for silicon, in Fig. 2 we show the LPD of the density and of the xc potential along a path (see the inset to the second panel). The QMC-derived xc potential differs from the LDA and PBE especially on the sodium atoms, where the density shows rapid changes. At first sight, however, and as in the case of silicon, it is difficult to rationalize the differences between the three potentials. While it is exciting to see the numerically exact xc potential for real semiconductors and insulators, it is useful to switch to a representation that highlights the essence of the difference, in order to gain more insight.

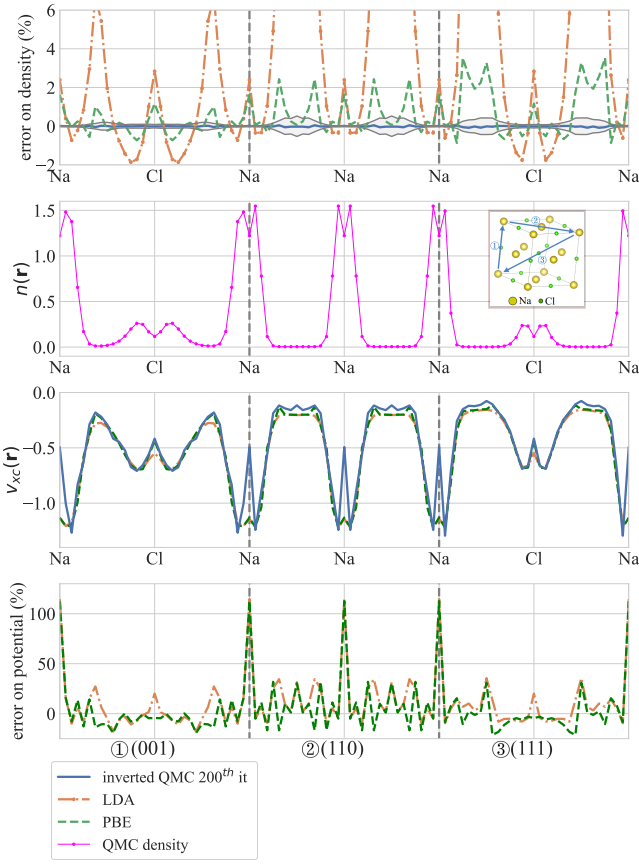


FIG. 2. Iterative inversion following Eq. (1) with the QMC density n_{QMC} of NaCl as reference density along the same path across the unit cell as in Ref.⁶⁹. The result of the QMC inversion is shown at $i = 200$. The MaAPE on the density at $i = 200$ compared to n_{QMC} is 0.29 %, and the MeAPE is 0.03%. Top panel: LPD of $n_{\text{QMC},200}$ (blue), self-consistent LDA n_{LDA} (orange), and PBE n_{PBE} (green) densities with respect to n_{QMC} . The grey area in the top panel indicates the stochastic error bar of the QMC density. Second panel: The QMC density n_{QMC} (thin magenta line). The inset shows the chosen path across the crystal from Ref.⁶⁹. Third panel: $v_{\text{xc},200}$ (blue), $v_{\text{xc}}^{\text{LDA}}$ (orange) and $v_{\text{xc}}^{\text{PBE}}$ (green). The averages of the potentials are aligned. Bottom panel: LPD of xc potentials with respect to $v_{\text{xc}}^{\text{QMC},200}$ for LDA (orange) and PBE (green).

B. Non-local dependence of the KS exchange-correlation functional on the density

In the LDA, $v_{\text{xc}}(\mathbf{r})$ is a monotonic function of $n(\mathbf{r})$. The exact KS potential is a functional of the density everywhere, which means that it can take different values in different points \mathbf{r} where the density, instead, is the same. This expresses the fact that $v_{\text{xc}}(\mathbf{r})$ depends not just on the local density, but also on the environment. In order to highlight how the true v_{xc} differs from a function of the local density, we create a map of $v_{\text{xc}}(\mathbf{r})$ with respect to $n(\mathbf{r})$: for each point \mathbf{r} in real space, we add a point $[v_{\text{xc}}(\mathbf{r}) \leftrightarrow n(\mathbf{r})]$ to Fig. 3 and Fig. 4 for silicon and NaCl,

respectively. In the case of the LDA, this plot shows the universal function $v_{\text{xc}}(n)$, the same for silicon and NaCl, which is identical to the function in the HEG. Beyond the LDA, different environments may change this function, such that it is different for different materials. Moreover, in one and the same material the presence of different environments may lead to the presence of more than one function, and finally, if the result is very sensitive to details, one might find it difficult to detect anything like a limited number of functions. All these effects are possible signatures of the non-local dependence of $v_{\text{xc}}(\mathbf{r})$ on the density, and being able to discern them, and to characterize different environments, may give precious input for further modeling of v_{xc} .

The maps in Fig. 3 and 4 contain the results of LDA, PBE and QMC. In silicon, the PBE result (upper panels of Fig. 3) is dominated by a simple monotonic function, but it is slightly steeper than the universal LDA function. Moreover, the result appears to be a little more scattered. Finally, a new branch appears at low densities. For more insight, the colors reflect, respectively, the modulus of the local gradient of the density (left panels) and the KS kinetic energy density defined as $\tau(\mathbf{r}) = \frac{1}{2} \sum_i^{\text{occ}} |\nabla \phi_i(\mathbf{r})|^2$, where ϕ_i are KS orbitals (right panels). The QMC xc potential in the bottom panels is more blurred than the PBE result, but this may be due to the noisy density, since test calculations using the LDA density augmented with some Gaussian noise lead to similar scattering, as shown in App. D. The overall shape and branches of the QMC xc potential, instead, are significant. Similarly to the PBE, one can identify a dominant curve, and, with respect to the LDA, two main changes are seen: the curve is steeper than that of the LDA, and at low densities an additional branch appears. The change in slope of the main branch with respect to the LDA goes in the same direction as in the PBE result, and it is even more pronounced. Also the branching happens in a similar region as in the case of PBE. However, the branch departs in the opposite direction.

As in the case of PBE, it is characterized by a very different gradient and kinetic energy density with respect to the main branch at the same local density. Indeed, the region in space where the potential lies on the extra branch is close to the center of the atoms, where the density varies rapidly. It should therefore be noted that it will be particularly sensitive to details of the pseudopotential. This, together with the fact that the inversion error on the density is largest on the atoms (see Fig. 10 in the Appendix), which then also influences the large density gradients in the vicinity, suggests that the wrong direction of the PBE branch observed here would deserve more studies including many more QMC datasets using different pseudopotentials and including different materials, which is beyond the scope of the present work. The changed slope of the main branch, instead, happens over the complete range of densities and should be a feature of silicon independent of the pseudopotential and other ingredients of the calculation.

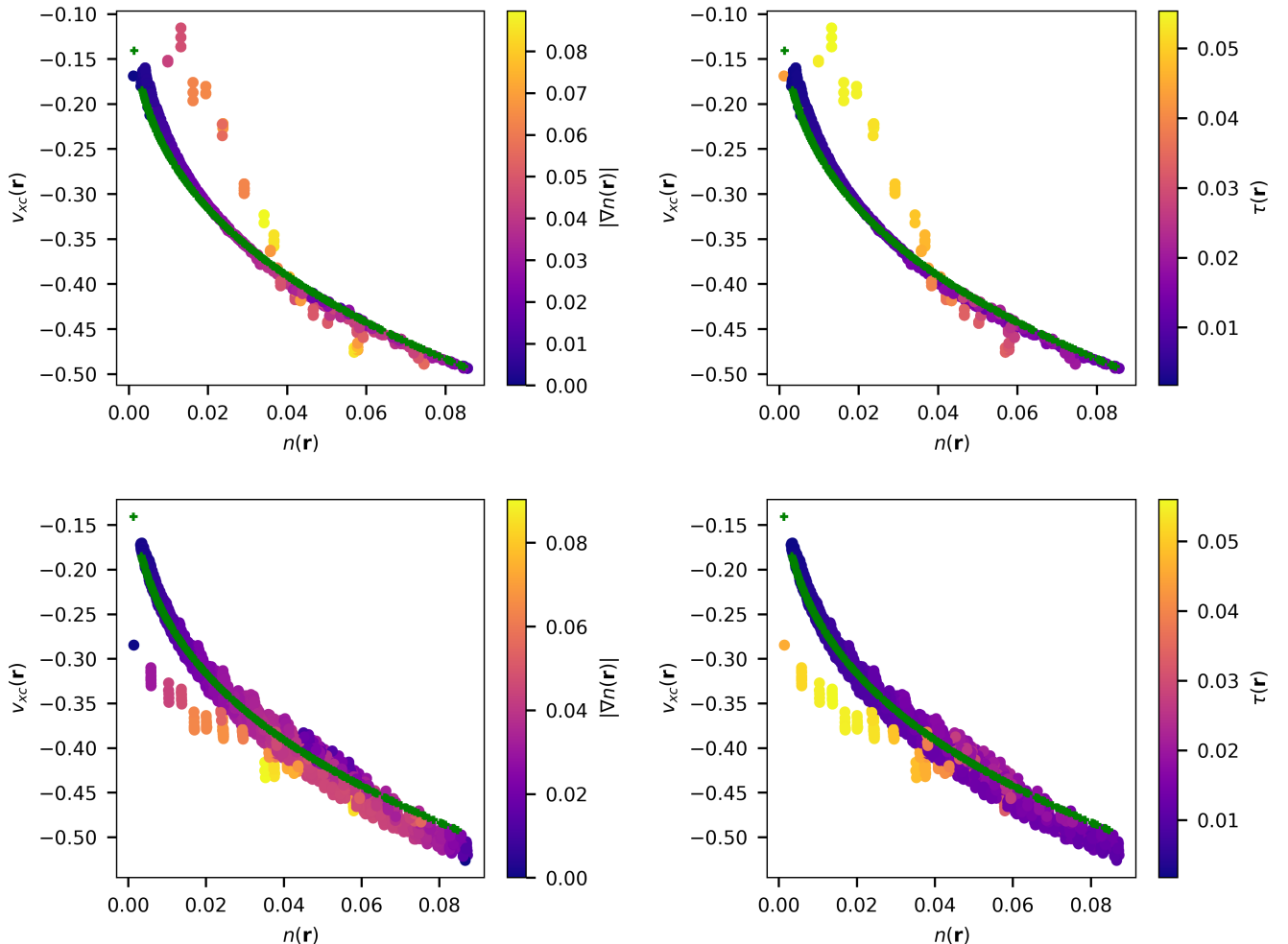


FIG. 3. Map of the xc potential of silicon with respect to the local density at all points in the unit cell. Color codes reflect the modulus of the local gradient of the density (left column) or the local kinetic energy density (right column). Upper figures are for PBE and bottom figures for QMC. The LDA is shown in green.

The modifications of the different branches with respect to the LDA v_{xc}^{LDA} may be translated in different ways, for example: $v_{xc}^e(\mathbf{r}) = F^e(n(\mathbf{r}))v_{xc}^{\text{LDA}}(n(\mathbf{r}))$ with a correction factor F^e that depends on the local density and on an environment e , which must be characterized. Another possibility would be $v_{xc}^e(\mathbf{r}) = v_{xc}^{\text{LDA}}(\mathcal{F}^e(n(\mathbf{r})) \times n(\mathbf{r}))$. The GGAs, for example, are an attempt to characterize the environment by the local gradient of the density (see, e.g.,⁷¹). Our results motivate further search for improved approximations of the true *functional* that can be expressed as *functions* of a limited number of parameters, such as the local density and its gradients.

Consistently with the fact that the QMC density for NaCl is less noisy than in the case of silicon, the map for NaCl in Fig. 4 (bottom panels) shows less scattering. As for silicon, we find a main branch that corresponds to a modified LDA. Moreover, there is an additional branch at low densities and another branch at high density, both

characterized by differences in the gradient or kinetic energy density. The analogous secondary branches for PBE (see upper panels) are less pronounced. The inset in the lower right panel also shows the QMC density along part of the path. Numbers indicate to which locations selected data points correspond. For example, data point 1 on the additional high-energy branch corresponds to the potential on the sodium atom, with an environment where the density is very quickly varying, which explains why the LDA completely fails. Data point 2, instead, corresponds to a place with similar density but located in a more gentle environment, although the gradient of the density is significant. As expected, in this point we are on the main branch, which is, however, modified with respect to the LDA.

Similarly, points 3 and 4 on the chlorine atom explain the extra branch at lower density. These results show that the potential-density relation presented as maps such as the one in Figs. 3 and 4 may give further in-

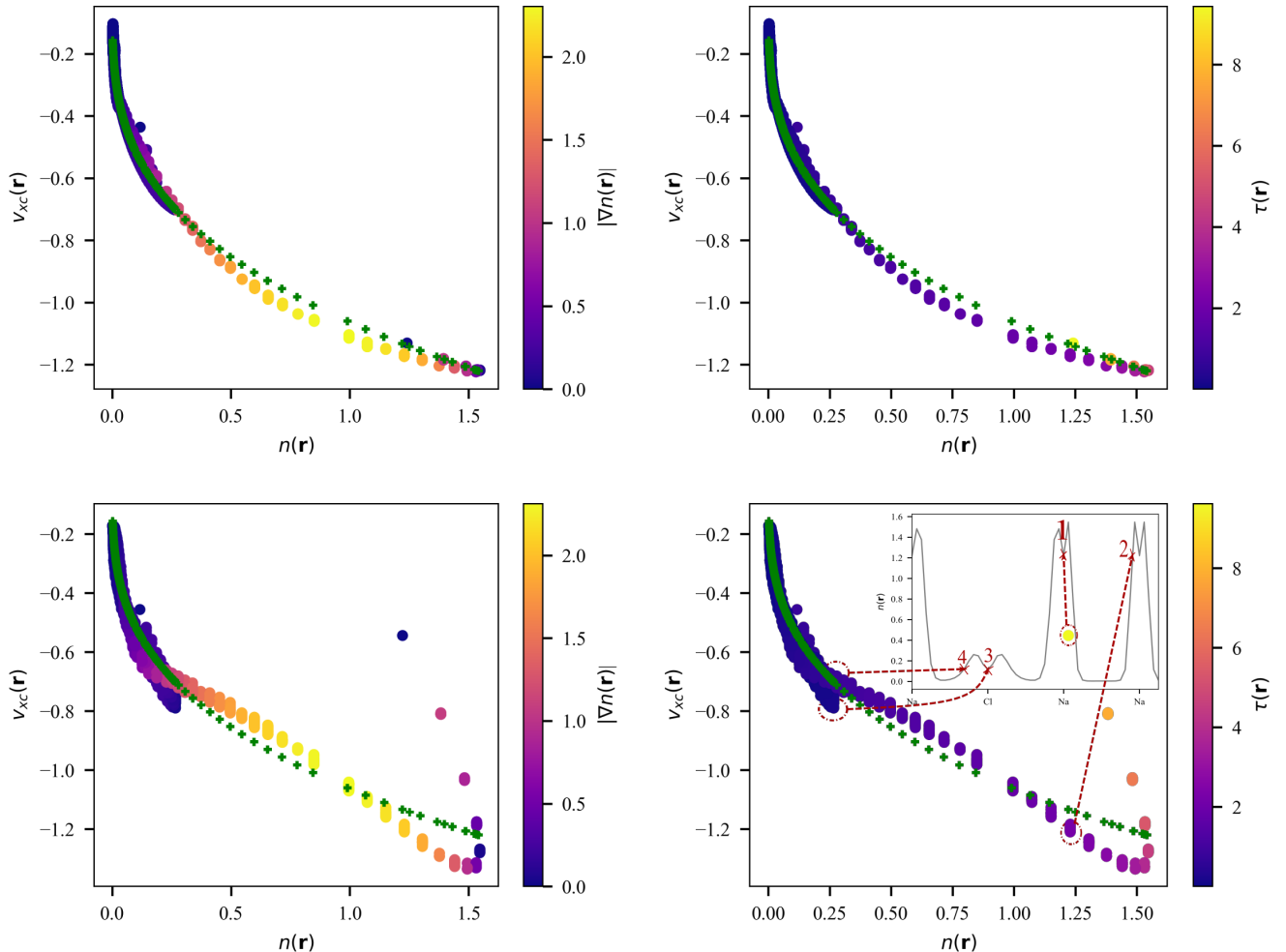


FIG. 4. Same as Fig. 3, for NaCl. Note the much larger range for $n(\mathbf{r})$ here. Upper panels are for PBE and bottom panels for QMC. The LDA is shown in green. The inset in the bottom right panel shows the QMC density along a part of the path across the unit cell.

sight about the most efficient way to introduce correction factors, and about the most important features distinguishing different environments, which could eventually be combined with machine learning approaches⁷².

C. Significance of the Kohn-Sham potential

A striking observation from the iteration procedure is that very different v_{xc} can yield very similar densities.^{73–75} This becomes evident when one starts from the noisy LDA (see App. D 2) or the QMC data for silicon and pushes the iteration process well inside the region where the MeAPE of the density does not improve any more (see Fig. 6 in the Appendix). While also the MaAPE of the density remains modest, of the order of, or smaller than, the noise itself, the xc potential at higher iterations develops strong spikes when the reference density is noisy. In order to quantify the effect, the upper

panel of Fig. 5 shows the MaAPE of the xc potential as a function of the iteration i , calculated with respect to the smooth potential that is obtained at $i_0 = 20$ in the case of QMC, and $i_0 = 24$ in the case of noisy LDA (The potentials themselves are shown in the Appendix, in the second panel of Fig. 10). In both cases, this deviation from the smooth potential shows strong variations. This raises the question what will happen to KS observables other than the density: even though, as discussed above, these do not by themselves have direct physical meaning in an exact sense, they can still be seen as an approximation to the physical quantities^{76,77}, and they are frequently used as starting points for calculations in a more appropriate framework, such as many-body perturbation theory⁷⁸. We therefore show in the bottom panel of Fig. 5 the direct KS band gap of silicon at Γ as a function of the number i of iterations at which the KS potential and corresponding density were calculated. The result converges very rapidly with i and remains stable, within

1 meV, over a wide range of iterations even after the potential has developed huge spikes. This means that very different xc potentials can yield not only very similar densities, but also very similar KS observables more in general. Moreover, the figure shows that the gaps corresponding to clean and noisy LDA densities are almost indistinguishable, i.e., the noise does not affect KS observables. It confirms the statement, mostly based on findings from low-dimensional systems, that examining the xc potential alone is not sufficiently meaningful^{73–75}. It also suggests that an effort is needed to distinguish in the KS potential crucial features, which must be contained in good functionals, from others that may be quantitatively strong in the potential, but insignificant for its effects.

D. Kohn-Sham approximation to the band gap

The study of the KS band gap is interesting by itself, since there is long-standing debate concerning the difference between observables in the real and KS auxiliary systems. In absence of knowledge of the exact Kohn-Sham potential, it was not possible to distinguish between the discrepancies due to approximations of the functional, and those due to the difference between the (even exact) Kohn-Sham system itself and the real material. Precious hints were already given by work on model systems; for example, Knorr and Godby^{34,35} determined the xc potential by inversion from the density of a finite one-dimensional model semiconducting wire that was then extrapolated to infinite length. Most of the band gap error was shown to be due to the fact that the exact KS eigenvalue gap differs from the fundamental electron addition and removal gap, and not due to approximations. Indeed, the KS eigenvalue gap calculated at fixed particle number disregards the derivative discontinuity of the exact xc potential upon change of particle number^{12–14}. Since the numerically exact density and/or xc potential could be obtained only for very few, low-dimensional, systems, several studies used the link between the xc potential and the self-energy given by the Sham-Schlüter equation¹³ in order to extract v_{xc} from the self-energy. These include work on a two-plane wave model^{13,79}, the surface barrier for semi-infinite jellium⁸⁰, finite systems^{21,81–83}, and the study of several real semiconductors and insulators^{18,20–26}. These studies confirmed that the error inherent in using Kohn-Sham eigenvalues instead of true electron addition and removal energies is significant. However, the approaches used to determine the potential involved themselves approximations whose quantitative impact on the findings are not known: first, the Sham-Schlüter equation was linearized in all studies; second, the self-energy itself was approximated in many-body perturbation theory, mostly on the GW⁸⁴ level. With the present work, we finally do have an almost numerically exact Kohn-Sham potential at hand for real materials, and we can therefore draw

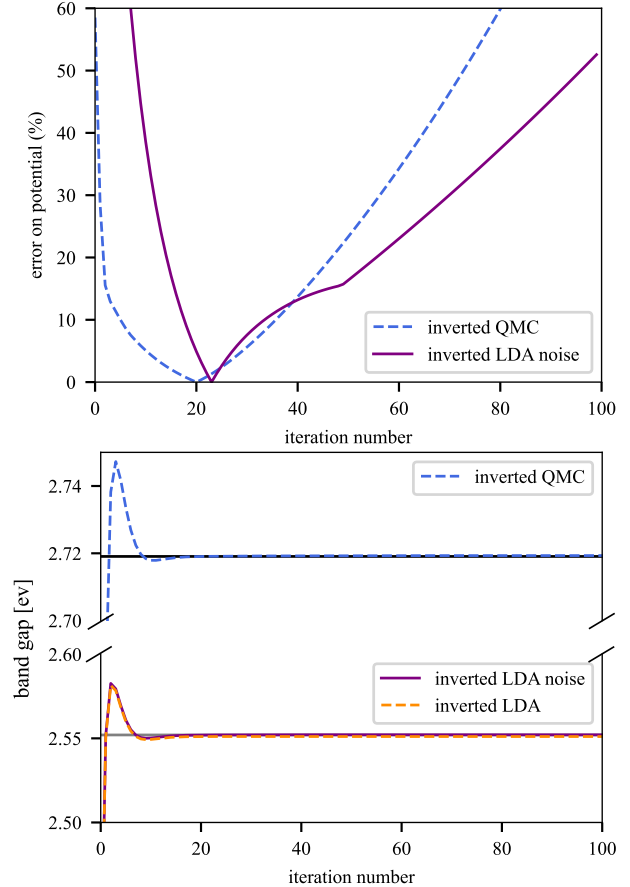


FIG. 5. (Upper panel) The xc potential of silicon MaAPE as a function of iteration i , calculated with respect to the result at $i_0 = 20$ for QMC (dashed blue line) and with respect to the result at $i_0 = 24$ for noisy LDA (purple line). (Bottom panel) Direct KS band gap of silicon at Γ : convergence with number of iterations for clean and noisy LDA (purple and dashed orange lines, respectively, overlapping almost entirely), and QMC (dashed blue line). Horizontal lines are the KS gap for the clean LDA (grey) at 2.55 eV, and the best estimated result from the iterative procedure for QMC (black) at 2.72 eV. Note the break in vertical scale.

definite conclusions concerning the band structure, and in particular the band gap, of standard semiconductors and insulators.

Results for the converged band gaps of silicon and NaCl are shown in Table I. For silicon, our numerically exact minimum indirect KS band gap is 0.69 eV, about 40 % larger than the KS gap of 0.49 eV calculated in LDA, and significantly smaller than the experimental gap⁸⁵ of 1.17 eV. The PBE gap of 0.66 eV is close to the QMC-derived value. The direct band gap opening of QMC with respect to LDA is analogously 0.17 eV at Γ and 0.12 eV at X. In NaCl, the situation is similar, with the QMC-derived gap about 14% larger than the LDA one, and only 3% larger than the PBE gap. The 5.25 eV

	Si		NaCl
	indirect	direct at Γ	direct at Γ
QMC derived	0.69	2.72	5.25
PBE	0.66	2.60	5.08
LDA	0.49	2.55	4.59
Exp.	1.17 ⁸⁵	3.05 ⁸⁷	8.5 ⁸⁶
		3.40 ⁸⁵	

TABLE I. KS minimum band gaps and direct band gaps at Γ (eV) in comparison with experimental photoemission gaps from Refs.^{85–87}.

QMC-derived KS gap is again much smaller than the 8.5 eV experimental gap⁸⁶. The bandwidths do not change in a noteworthy way with respect to LDA (or PBE): in silicon the QMC valence bandwidth is reduced by 0.1 eV compared to LDA (and 0.05 eV compared to PBE), while in NaCl the QMC bandwidth is 0.15 eV smaller than LDA and 0.04 eV larger than PBE.

Our QMC derived KS gaps confirm the conclusion of Ref.^{18,20} and thus definitely highlight the fact that a good multiplicative KS potential will not yield a “good” eigenvalue band gap in solids. Overall, the band gap is an excellent illustration for the fact that the exact Kohn-Sham system is an auxiliary system designed to yield the density in principle exactly, but for other observables, it can only give an approximation.

IV. CONCLUSION

In conclusion, we have shown that a simple algorithm allows one to obtain the Kohn-Sham xc potential for periodic semiconductors and insulators, given their ground state density. The precision that can be obtained is limited by the quality of the input data. Here, we use densities taken from AFQMC calculations, and the limiting factor is the stochastic noise. Nevertheless, meaningful results are obtained, with an error bar smaller than the difference between the resulting potentials and their LDA or PBE counterparts, which allows us to safely draw conclusions. In particular, for the materials studied here, namely bulk silicon and NaCl, the xc potential *functional of the density everywhere* can be represented in terms of two or three *functions of the local density*, each of which is determined by a specific environment. These environments appear to be characterized by the local gradient of the density or, even more clearly, by the local kinetic energy density. The function that represents most of the data points is close to the LDA, but with slight material-dependent deviations. PBE also predicts deviations and the existence of the additional functions, although it does not always describe them well. On the other hand, our results clearly illustrate that very different potentials may lead to very similar densities, and more generally, to very similar KS observables. In particular, the KS band gap

converges rapidly with the number of iterations of the inversion process, while the xc potential still undergoes violent modifications. More work is needed to discern important features of the xc potential from those that do not influence KS observables; sum rules and other exact constraints may be helpful for this^{8–11}. Our results for the KS band gap confirm previous conjectures based on model systems and/or many-body perturbation theory, which predict that the exact KS band gap is closer to the LDA one than to the measurable electron addition and removal gap, in other words, that the derivative discontinuity of the true xc potential is sizable. Still, the LDA error is non negligible, whereas PBE predicts the exact KS gap with an error of less than 5% for the materials studied here. Our work highlights directions for the improvement of density functionals, stressing the need for, and usefulness of, QMC calculations of the density in many more materials.

V. ACKNOWLEDGEMENTS

Fruitful discussions with Kieron Burke and Rex Godby are acknowledged. S.C. was supported by the U.S. Department of Energy (DOE) under Grant No. DE-SC0001303, and by the Center for Computational Quantum Physics, Flatiron Institute. The Flatiron Institute is a division of the Simons Foundation.

Appendix A: Computational details

We have adopted the same computational parameters (lattice constants, cutoff energies and k-point grids) and pseudopotentials as in Ref.⁶⁹. Following Ref.⁶⁹, all the LDA, PBE and QMC results have been obtained with the same optimized norm-conserving LDA pseudopotentials⁸⁸. We have employed the Abinit code⁸⁹ and verified that it gives the same numerical results as the Quantum Espresso code⁹⁰ used in Ref.⁶⁹. The KS inversion algorithm has been implemented in our own KS python code, which is interfaced with the Abinit code.

Appendix B: Accuracy of the algorithm

To illustrate the reliability of the inversion algorithm, it is instructive to examine a case where the density-potential relation is well known; here, we choose the LDA. This means that in Eq. (1), $n_{\text{ref}} = n_{\text{LDA}}$ is the density obtained in a standard LDA Kohn-Sham self-consistent calculation with exchange-correlation potential $v_{\text{xc}}^{\text{LDA}}$ at convergence. Ideally, from the iteration procedure for $i \rightarrow \infty$ we should find $v_{\text{xc}}^{\text{LDA},i} \rightarrow v_{\text{xc}}^{\text{LDA}}$ and $n_{\text{LDA},i} \rightarrow n_{\text{LDA}}$. Fig. 6 and 7 show results for silicon.

In Fig. 6 (upper panel) the Maximum (over the unit cell) of the Absolute value of the Percentage Error (MaAPE) of the density $n^{\text{LDA},i}$ compared to the LDA

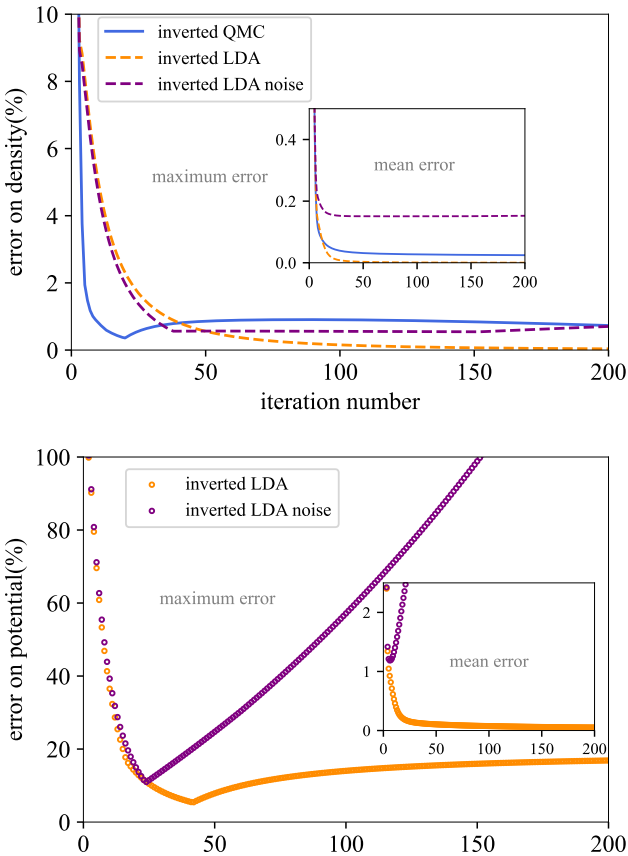


FIG. 6. Errors of the iteration procedure as a function of number of iterations i in silicon. Top panel: MaAPE of the density for the inverted LDA (orange), inverted noisy LDA (purple) and QMC (blue) xc potentials. Each inverted density is compared to its corresponding reference result. In the inset: MeAPE of the density for the inverted LDA, noisy LDA and QMC xc potentials. Bottom panel: MaAPE of the xc potential for the inverted LDA (orange) and inverted noisy LDA (purple). In these cases the error is defined with respect to v_{xc} of KS LDA, since the xc potential that yields the noisy density is unknown. In the inset: MeAPE of the xc potential for the inverted LDA and inverted noisy LDA potentials.

one, $100 \times \max_{\mathbf{r}} |1 - n^{\text{LDA},i}(\mathbf{r})/n_{\text{LDA}}(\mathbf{r})|$, is shown as a function of the iteration number i . It decreases smoothly and very fast. The same is true for the Mean Absolute (over the unit cell) Percentage Error (MeAPE), given in the inset.

In Fig. 7 snapshots for the errors on density and v_{xc} are presented. The upper panel gives $100 \times (1 - n^{\text{LDA},i}(\mathbf{r})/n_{\text{LDA}}(\mathbf{r}))$, the Local Percentage Difference (LPD) along a path through the unit cell (the same as in Ref.⁶⁹) of the density at $i = 500$ iterations (orange dashed line) with respect to the LDA one. In the scale of the figure, it is close to zero everywhere: it is largest, with a maximum of $6.55 \times 10^{-4} \%$, in places of low LDA density, shown by the thin magenta line in the middle panel. The LPD of the potential is shown in the bottom

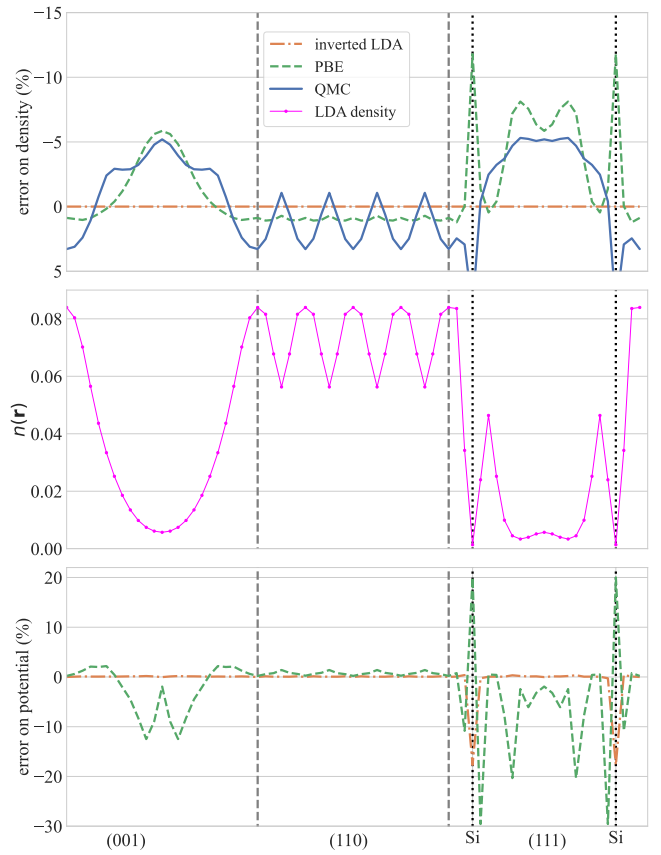


FIG. 7. Upper panel: The LPD of the density: in orange, LPD of $n^{\text{LDA},500}$ with respect to n_{LDA} (where the MaAPE is $6.55 \times 10^{-4} \%$); in green LPD of the self-consistent PBE and in blue QMC densities with respect to n_{LDA} . Middle panel: Self-consistent LDA density n_{LDA} (thin magenta line). Lower panel: LPD of $v_{xc}^{\text{LDA},500}$ (orange) and self-consistent PBE potential v_{xc}^{PBE} (green) with respect to v_{xc}^{LDA} .

panel of Fig. 7. Because of the arbitrary shift, only a comparison of the variations of the potential is pertinent. Indeed, during the iterations the average potential continuously moves upwards. The figure has been obtained by re-aligning at the end of the iterations the average potentials. This requires a final downwards shift of the iterative potential of 0.06 Hartree. Again, the maximum error is found in places of lower density, here in particular on the atoms. The LPD is significantly larger for the potential than for the density, and it can be clearly detected on the atoms. This can also be appreciated in Fig. 6 (bottom panel), where the open circles in the main panel give the MaAPE and MeAPE on the xc potential as a function of iterations. In order to illustrate that the remaining errors are small enough to make discussions meaningful, the errors in Fig. 7 are compared to the difference between two different functionals, here, between PBE and LDA (see green lines). The top panel contains the LPD of the PBE density with respect to the LDA self-consistent one, $100 \times (1 - n_{\text{PBE}}(\mathbf{r})/n_{\text{LDA}}(\mathbf{r}))$. This difference can be seen very clearly, since it is more than 10^4 times larger than

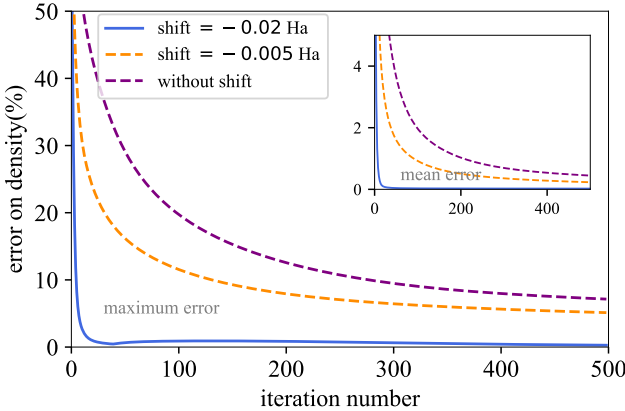


FIG. 8. Silicon: error of the inverted QMC density as a function of the iteration number for three different choices of the shift of the starting point. The starting point is $0.1v_{xc}^{LDA} + \text{shift}$.

the inversion error. The LPD of the PBE with respect to the LDA xc potential, $100 \times (1 - v_{xc}^{\text{PBE}}(\mathbf{r})/v_{xc}^{\text{LDA}}(\mathbf{r}))$, can be found in the bottom panel. Differences can be seen throughout the path, although regions of lower density show larger differences. These differences are, though slightly larger, of the same order as the differences in the density. Except for immediate vicinity of the atoms, they are much larger than the error of the inversion, like in the case of the density. This demonstrates that the inversion yields meaningful results, with an error bar that is much smaller than the differences of interest.

Appendix C: Further to the stability of the results

It is important to note that the results of the inversion do not depend on the starting point. This is true both for the shape and for the average value of the starting potential. The latter is important for the convergence behavior: Fig. 8 shows that a value of the initial shift which guarantees that the potential does not change sign improves the convergence for silicon significantly. Fig. 9 shows results obtained for a starting point corresponding to different fractions of v_{xc}^{LDA} : the scatter plot of silicon shows stability both of the main and of the extra branch.

Appendix D: Inversion starting from noisy densities

1. Inversion using as reference density the QMC density of silicon

With respect to the density obtained from a self-consistent KS calculation, the QMC density is more noisy. Here, we will examine the consequences on the inversion procedure for silicon, where the effect is more pronounced than in NaCl.

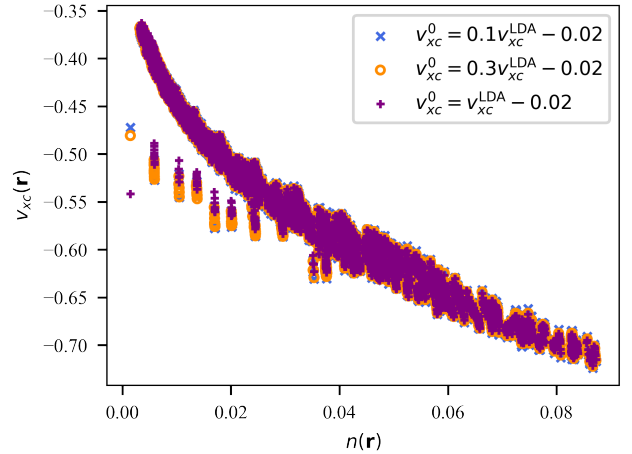


FIG. 9. Map of the xc potential of silicon with respect to the local density for three different choices of the starting point. The three xc potentials have the same MeAPE of 0.02 %. This precision is reached at $i = 11, 20$ or 38 when the starting point is a shifted v_{xc}^{LDA} , $0.3v_{xc}^{\text{LDA}}$ or $0.1v_{xc}^{\text{LDA}}$, respectively.

The first interesting fact is that the MaAPE of the density as a function of the number of iterations i , given by the blue curve in Fig. 6 (upper panel), shows an overall decrease, but with a pronounced minimum at $i = 20$. At this point, it has decreased to 0.38%. The minimum is followed by a modest increase, after which the error decreases again monotonously. Instead, as the inset in Fig. 6 shows, in correspondence to the minimum the MeAPE reaches a plateau of about 0.02% and a better precision cannot be reached. For this reason, the inversion error remains larger than what we obtained in the case of the inverted LDA, by about a factor 500 for the MaAPE and 1000 for the MeAPE.

Of course, one could think to continue the iterations, since Fig. 6 shows that the MaAPE could be decreased further. However, the fact that a plateau is reached in the MeAPE anticipates that one might encounter problems when doing so. The blue curve in the upper panel of Fig. 10 shows the density from the QMC inversion at $i = 500$, where the MaAPE has decreased from 0.38% to 0.21 %. Indeed, the error is now further away from the QMC error bar in the most critical points along the path, with respect to the $i = 20$ result shown in Fig. 7. Also the MeAPE has decreased from 0.04 % at $i = 20$ to 0.02 % at $i = 500$. However, the xc potential obtained from the QMC inversion, shown in the bottom panel of Fig. 10 (blue curve), is no longer smooth. It develops spikes that become even more pronounced when one iterates further, while still decreasing the MaAPE on the density, but with a quite constant MeAPE, which points to a mere redistribution of errors (see Fig. 11 for illustration).

Visibly, the algorithm does not succeed in improving the result any further and introduces unexpected features when trying to do so. Difficulties with the inversion pro-

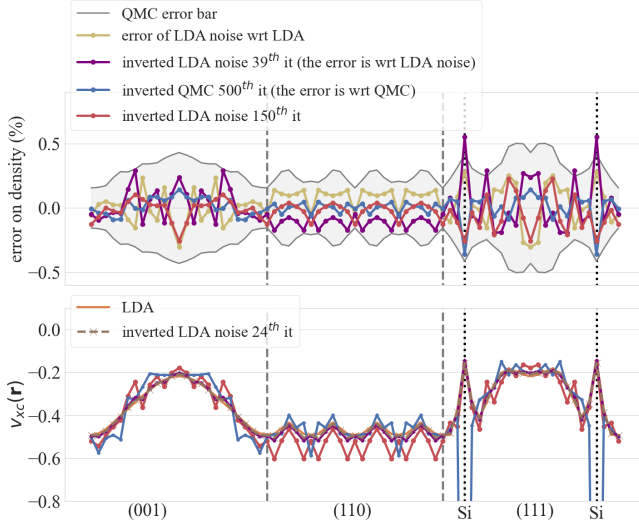


FIG. 10. Relation between noise and errors of the iterative procedures that use n_{QMC} or $n_{LDA+noise}$ as reference densities. Top panel: In yellow, LPD of the LDA density from the KS calculation decorated with a point-wise Gaussian noise $n_{LDA+noise}$ with respect to the clean LDA density n_{LDA} . The noise lies within the stochastic error bar of the QMC calculation (grey area). In purple, LPD of $n_{LDA+noise,39}$ at the iteration $i = 39$, where the MaAPE on the density with respect to $n_{LDA+noise}$ has its first minimum. Here, the MaAPE is 0.56%, and the MeAPE is 0.15%. In red, LPD of $n_{LDA+noise,150}$ at the iteration $i = 150$, where the MaAPE is 0.54%. In blue, LPD of $n_{QMC,500}$ at the iteration $i = 500$, where the MaAPE is 0.21% and the MeAPE is 0.02%, with respect to n_{QMC} . Bottom panel: the LDA v_{xc}^{LDA} potential (orange) is compared to the xc potentials obtained by inversion of the QMC density $v_{xc}^{QMC,500}$ (blue), and by inversion of the noisy LDA density $v_{xc}^{LDA+noise,24}$ (brown dashed line), $v_{xc}^{LDA+noise,39}$ (purple), and $v_{xc}^{LDA+noise,150}$ (red) at $i = 150$.

cedure have also been reported for finite systems, and they have been attributed to the finite basis set which may introduce an inconsistency between density and external potential^{49–53}. In the present work, as we have verified, the results are sufficiently well converged to exclude basis set problems, but there is another issue: the QMC density has stochastic noise.

2. Effect of noise on top of the LDA density

In order to show that the QMC stochastic noise may be responsible for the observed behavior, we have taken the LDA density $n(\mathbf{r})$ and added point-wise Gaussian noise, which is obtained from a normal distribution with mean zero and standard deviation given by the characteristic AFQMC statistical error bar scaled by $n(\mathbf{r})$. To appreciate what this means, the yellow curve in the upper panel gives the relative difference of the noisy LDA density with respect to the clean one. Fig. 10 shows results for the inversion starting from this new refer-

ence density. The error of the inversion of the noisy LDA data is displayed in Fig. 6 (upper panel, purple curve). It behaves similarly to the QMC inversion error: the MaAPE decreases rapidly and reaches a minimum, from whereon a slight increase followed by a decrease is noted. The MeAPE, instead, reaches a plateau. The inversion error on the density is given by the purple curve in the upper panel of Fig. 10, representing the LPD $100 \times (1 - n_{LDA+noise,39}(\mathbf{r})/n_{LDA+noise}(\mathbf{r}))$ at 39 iterations. It is of similar magnitude as the noise itself, as in the QMC case. Iterating further to $i = 150$ (red), only a slight smoothing of the error on the density is observed. The bottom panel of Fig. 10 shows xc potentials: the red curve is the xc potential resulting from inversion of the noisy LDA data at $i = 150$. It has spikes that are of the same order as those of $v_{xc}^{QMC,500}$ (blue curve) and that are in percentage orders of magnitude larger than the noise of the density, again as in the case of $v_{xc}^{QMC,500}$. With such an error bar, one would not be able to distinguish the LDA and QMC potentials. By way of contrast, the xc potential resulting from the noisy LDA data but at only $i = 39$ iterations, where the MaAPE on the density has its minimum, shows only very small spikes (purple curve). The result is stable in the range of iterations preceding that minimum: the bottom panel also shows the result for $i = 24$ (brown dashed curve), with a virtually indistinguishable potential. Moreover, this potential is close to the clean LDA potential, given by the orange curve. In this range of iterations, we can consider the resulting potential to be reliable. The spikes that develop by iterating further, instead, may suffer from the fact that the noisy density and the KS LDA hamiltonian are not completely consistent, which means that a higher precision cannot be reached.

The observations concerning the behavior of the noisy LDA are strictly analogous to our QMC-based results. This gives strong evidence for the fact that the inversion problem of the QMC data after a certain number of iterations is indeed due to the stochastic noise of the QMC. Moreover, it suggests that a sufficiently reliable xc potential is obtained by taking the result in the range where a stable and relatively smooth potential is obtained, and before the MeAPE on the density stops to decrease. In the present case, this confirms the choice $i = 20$, for which the QMC xc potential is given in Fig. 1. In other words, this xc potential is, to the best of our knowledge, today's most precise estimate for the true xc potential of bulk silicon.

Finally, Fig. 12 confirms that the noise is at least partially responsible for the blurring of the QMC result observed in the map $[v_{xc}(\mathbf{r}) \leftrightarrow n(\mathbf{r})]$ in Fig. 3: inversion of the noisy LDA data leads to a more scattered potential, as shown in the inset of Fig. 12. The comparison of the result for $i = 24$ and $i = 39$ also shows that it remains essentially a scattered version of the clean LDA result, with a blurring according to the number of iterations, whereas no additional features are caused by the noise. In the main panel, we compare different iterations of the

QMC result. Also in this case higher i leads to stronger blurring, but the extra branch is confirmed to be a stable feature.

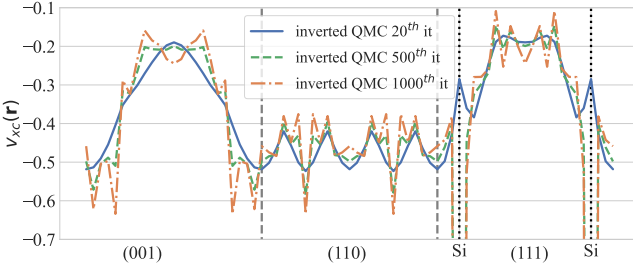


FIG. 11. Exchange-correlation potentials obtained by inversion of the QMC density of bulk silicon, at three different iteration steps. All three potentials yield a very similar, accurate density. The MeAPE of the density is 0.04% at $i = 20$, 0.02 % at $i = 500$, and the same value at $i = 1000$. For the MaAPE, we get 0.38% at $i = 20$, 0.21% at $i = 500$, and 0.18% at $i = 1000$.

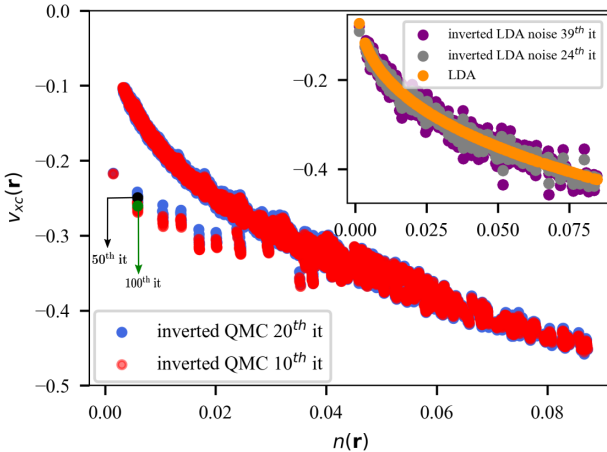


FIG. 12. Map of the xc potential versus the local density in silicon. Main panel: Results of the inversion of QMC for different i . Each v_{xc} is plotted against its own density. QMC inversion results are shown at 10 (smooth potential) and 20 (minimum of MaAPE of the density) iterations. For one density below 0.01, additional results at $i = 50$ and $i = 100$ are given, to illustrate the stability of the extra branch. In the inset, KS LDA is compared to the inversion of noisy LDA at 24 (smooth potential) and 39 (minimum of MaAPE of the density) iterations.

3. Additional results for NaCl

For completeness, we investigate the issue of noise also in NaCl. Since the QMC error bar is smaller in this case, results can be obtained with higher accuracy. We compare in Fig. 13 the inversion behavior of clean LDA,

of QMC and of LDA with a noise displayed in Fig. 14. The noise has similar effects as in the case of silicon. The final precision for the QMC result is higher than in silicon because the stochastic noise is smaller in regions of high density.

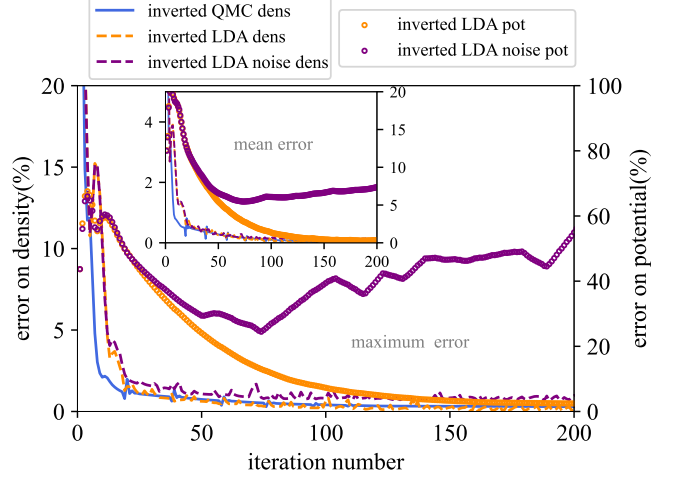


FIG. 13. Same as Fig. 6, but for NaCl. Again, the starting v_{xc} is 30% LDA, but here with a shift of -0.4 Hartree.

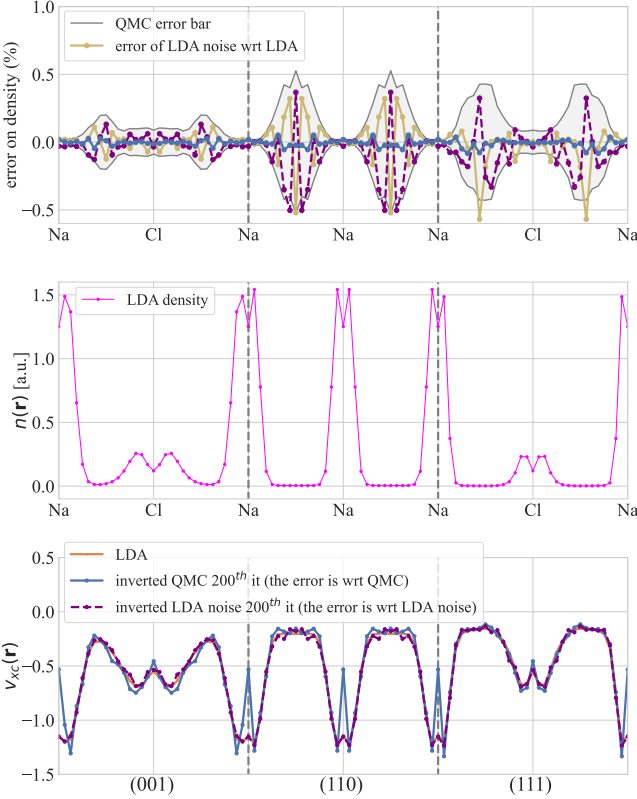


FIG. 14. Analog of Fig. 10, but for NaCl. Here spikes in noisy LDA and QMC are less developed than in the case of silicon. Note that the QMC error bar is smaller than in the case of silicon, in particular in regions of significant density.

¹ P. Hohenberg and W. Kohn, Phys. Rev. **136**, B864 (1964).
² W. Kohn and L. J. Sham, Phys. Rev. **140**, A1133 (1965).
³ W. Kohn, Rev. Mod. Phys. **71**, 1253 (1999).
⁴ R. M. Martin, *Electronic Structure: Basic Theory and Practical Methods* (Cambridge University Press, 2004).
⁵ D. M. Ceperley and B. J. Alder, Phys. Rev. Lett. **45**, 566 (1980).
⁶ M. G. Medvedev, I. S. Bushmarinov, J. Sun, J. P. Perdew, and K. A. Lyssenko, Science **355**, 49 (2017).
⁷ A. D. Becke, The Journal of Chemical Physics **156**, 214101 (2022).
⁸ J. P. Perdew and W. Yue, Phys. Rev. B **33**, 8800 (1986).
⁹ J. P. Perdew, K. Burke, and M. Ernzerhof, Phys. Rev. Lett. **77**, 3865 (1996).
¹⁰ J. P. Perdew, A. Ruzsinszky, G. I. Csonka, O. A. Vydrov, G. E. Scuseria, L. A. Constantin, X. Zhou, and K. Burke, Phys. Rev. Lett. **100**, 136406 (2008).
¹¹ J. Sun, A. Ruzsinszky, and J. P. Perdew, Phys. Rev. Lett. **115**, 036402 (2015).
¹² J. P. Perdew, R. G. Parr, M. Levy, and J. L. Balduz, Phys. Rev. Lett. **49**, 1691 (1982).
¹³ L. J. Sham and M. Schlüter, Phys. Rev. Lett. **51**, 1888 (1983).
¹⁴ J. P. Perdew and M. Levy, Phys. Rev. Lett. **51**, 1884 (1983).
¹⁵ J. P. Perdew and A. Zunger, Phys. Rev. B **23**, 5048 (1981).
¹⁶ M. van Schilfgaarde, T. Kotani, and S. Faleev, Phys. Rev. Lett. **96**, 226402 (2006).
¹⁷ L. J. Sham and W. Kohn, Phys. Rev. **145**, 561 (1966).
¹⁸ R. W. Godby, M. Schlüter, and L. J. Sham, Phys. Rev. Lett. **56**, 2415 (1986).
¹⁹ R. W. Godby, M. Schlüter, and L. J. Sham, Phys. Rev. B **36**, 6497 (1987).
²⁰ R. W. Godby, M. Schlüter, and L. J. Sham, Phys. Rev. B **37**, 10159 (1988).
²¹ Y. M. Niquet and X. Gonze, Phys. Rev. B **70**, 245115 (2004).
²² M. Grüning, A. Marini, and A. Rubio, Phys. Rev. B **74**, 161103 (2006).
²³ M. Grüning, A. Marini, and A. Rubio, The Journal of Chemical Physics **124**, 154108 (2006).
²⁴ T. Kotani, J. Phys.: Condens. Matter **10**, 9241 (1998).

²⁵ J. Klimeš and G. Kresse, *The Journal of Chemical Physics* **140**, 054516 (2014).

²⁶ S. Riemelmoser, M. Kaltak, and G. Kresse, *The Journal of Chemical Physics* **154**, 154103 (2021).

²⁷ R. van Leeuwen and E. J. Baerends, *Phys. Rev. A* **49**, 2421 (1994).

²⁸ Q. Zhao, R. C. Morrison, and R. G. Parr, *Phys. Rev. A* **50**, 2138 (1994).

²⁹ Q. Wu and W. Yang, *The Journal of Chemical Physics* **118**, 2498 (2003).

³⁰ K. Peirs, D. Van Neck, and M. Waroquier, *Phys. Rev. A* **67**, 012505 (2003).

³¹ C. O. Almbladh and A. C. Pedroza, *Phys. Rev. A* **29**, 2322 (1984).

³² F. Aryasetiawan and M. J. Stott, *Phys. Rev. B* **38**, 2974 (1988).

³³ A. Görling, *Phys. Rev. A* **46**, 3753 (1992).

³⁴ W. Knorr and R. W. Godby, *Phys. Rev. Lett.* **68**, 639 (1992).

³⁵ W. Knorr and R. W. Godby, *Phys. Rev. B* **50**, 1779 (1994).

³⁶ C. J. Umrigar and X. Gonze, *Phys. Rev. A* **50**, 3827 (1994).

³⁷ O. V. Gritsenko, R. van Leeuwen, and E. J. Baerends, *Phys. Rev. A* **52**, 1870 (1995).

³⁸ D. J. Tozer, V. E. Ingamells, and N. C. Handy, *The Journal of Chemical Physics* **105**, 9200 (1996).

³⁹ N. Helbig, I. V. Tokatly, and A. Rubio, *The Journal of Chemical Physics* **131**, 224105 (2009).

⁴⁰ E. M. Stoudenmire, L. O. Wagner, S. R. White, and K. Burke, *Phys. Rev. Lett.* **109**, 056402 (2012).

⁴¹ D. Varsano, M. Barborini, and L. Guidoni, *The Journal of Chemical Physics* **140**, 054102 (2014).

⁴² T. W. Hollins, S. J. Clark, K. Refson, and N. I. Gidopoulos, *Journal of Physics: Condensed Matter* **29**, 04LT01 (2016).

⁴³ M. J. P. Hodgson, J. D. Ramsden, and R. W. Godby, *Phys. Rev. B* **93**, 155146 (2016).

⁴⁴ M. J. P. Hodgson, E. Kraisler, A. Schild, and E. K. U. Gross, *The Journal of Physical Chemistry Letters* **8**, 5974 (2017).

⁴⁵ J. Wetherell, M. J. P. Hodgson, L. Talirz, and R. W. Godby, *Phys. Rev. B* **99**, 045129 (2019).

⁴⁶ S. Nam, S. Song, E. Sim, and K. Burke, *Journal of Chemical Theory and Computation* **16**, 5014 (2020).

⁴⁷ A. Savin, C. Umrigar, and X. Gonze, *Chemical Physics Letters* **288**, 391 (1998).

⁴⁸ J. Li, N. D. Drummond, P. Schuck, and V. Olevano, *SciPost Phys.* **6**, 40 (2019).

⁴⁹ P. R. T. Schipper, O. V. Gritsenko, and E. J. Baerends, *Theoretical Chemistry Accounts* **98**, 16 (1997).

⁵⁰ M. E. Mura, P. J. Knowles, and C. A. Reynolds, *The Journal of Chemical Physics* **106**, 9659 (1997).

⁵¹ T. Heaton-Burgess, F. A. Bulat, and W. Yang, *Phys. Rev. Lett.* **98**, 256401 (2007).

⁵² C. R. Jacob, *The Journal of Chemical Physics* **135**, 244102 (2011).

⁵³ A. P. Gaiduk, I. G. Ryabinkin, and V. N. Staroverov, *Journal of Chemical Theory and Computation* **9**, 3959 (2013).

⁵⁴ D. S. Jensen and A. Wasserman, *International Journal of Quantum Chemistry* **118**, e25425 (2018).

⁵⁵ Y. Shi and A. Wasserman, *The Journal of Physical Chemistry Letters* **12**, 5308 (2021).

⁵⁶ I. G. Ryabinkin and V. N. Staroverov, *The Journal of Chemical Physics* **137**, 164113 (2012).

⁵⁷ Q. Ou and E. A. Carter, *Journal of Chemical Theory and Computation* **14**, 5680 (2018), pMID: 30216062.

⁵⁸ B. Kanungo, P. M. Zimmerman, and V. Gavini, *Nature Communications* **10**, 4497 (2019).

⁵⁹ A. Kumar, R. Singh, and M. K. Harbola, *Journal of Physics B: Atomic, Molecular and Optical Physics* **52**, 075007 (2019).

⁶⁰ A. Kumar and M. K. Harbola, *International Journal of Quantum Chemistry* **120**, e26400 (2020).

⁶¹ A. Kumar, R. Singh, and M. K. Harbola, *Journal of Physics B: Atomic, Molecular and Optical Physics* **53**, 165002 (2020).

⁶² T. J. Callow, N. N. Lathiotakis, and N. I. Gidopoulos, *The Journal of Chemical Physics* **152**, 164114 (2020).

⁶³ S. Nam, R. J. McCarty, H. Park, and E. Sim, *The Journal of Chemical Physics* **154**, 124122 (2021).

⁶⁴ J. Erhard, E. Trushin, and A. Görling, *The Journal of Chemical Physics* **0**, null (0).

⁶⁵ Y. Shi, V. H. Chávez, and A. Wasserman, *WIREs Computational Molecular Science* **n/a**, e1617.

⁶⁶ Given the pseudopotential. In other words, all discussions are valid because we have used the same hamiltonian, with a fixed LDA pseudopotential, for the valence electron problem throughout, including for the QMC calculations. A full all-electron v_{xc} would of course look different.

⁶⁷ S. Zhang and H. Krakauer, *Phys. Rev. Lett.* **90**, 136401 (2003).

⁶⁸ M. Motta and S. Zhang, *WIREs Computational Molecular Science* **8**, e1364 (2018).

⁶⁹ S. Chen, M. Motta, F. Ma, and S. Zhang, *Phys. Rev. B* **103**, 075138 (2021).

⁷⁰ Note that we have defined the error with opposite sign with respect to Ref.⁶⁹.

⁷¹ J. P. Perdew, J. A. Chevary, S. H. Vosko, K. A. Jackson, M. R. Pederson, D. J. Singh, and C. Fiolhais, *Phys. Rev. B* **46**, 6671 (1992).

⁷² B. Kalita, L. Li, R. J. McCarty, and K. Burke, *Accounts of Chemical Research* **54**, 818 (2021).

⁷³ A. Savin, F. Colonna, and R. Pollet, *International Journal of Quantum Chemistry* **93**, 166 (2003).

⁷⁴ M.-C. Kim, E. Sim, and K. Burke, *Phys. Rev. Lett.* **111**, 073003 (2013).

⁷⁵ A. Wasserman, J. Nafziger, K. Jiang, M.-C. Kim, E. Sim, and K. Burke, *Annual Review of Physical Chemistry* **68**, 555 (2017).

⁷⁶ D. P. Chong, O. V. Gritsenko, and E. J. Baerends, *The Journal of Chemical Physics* **116**, 1760 (2002).

⁷⁷ C. Filippi, C. J. Umrigar, and X. Gonze, *The Journal of Chemical Physics* **107**, 9994 (1997).

⁷⁸ R. Martin, L. Reining, and D. Ceperley, *Interacting Electrons: Theory and Computational Approaches* (Cambridge University Press, 2016).

⁷⁹ M. Lannoo, M. Schlüter, and L. J. Sham, *Phys. Rev. B* **32**, 3890 (1985).

⁸⁰ A. G. Eguiluz, M. Heinrichsmeier, A. Fleszar, and W. Hanke, *Phys. Rev. Lett.* **68**, 1359 (1992).

⁸¹ M. Hellgren and U. von Barth, *Phys. Rev. B* **76**, 075107 (2007).

⁸² M. Hellgren and U. von Barth, *The Journal of Chemical Physics* **132**, 044101 (2010).

⁸³ P. Bleiziffer, A. Heßelmann, and A. Görling, *The Journal of Chemical Physics* **139**, 084113 (2013).

⁸⁴ L. Hedin, *Phys. Rev.* **139**, A796 (1965).

⁸⁵ Landolt-Börnstein, *Numerical Data and Functional Relationships in Science and Technology*, New Series Group III, Subvolume B: II-VII and I-VII Compounds, Vol. 17 Pt A (Springer-Verlag, Berlin-Heidelberg, New York, 1982).

⁸⁶ R. T. Poole, J. G. Jenkin, J. Liesegang, and R. C. G. Leckey, Phys. Rev. B **11**, 5179 (1975).

⁸⁷ J. E. Ortega and F. J. Himpel, Phys. Rev. B **47**, 2130 (1993).

⁸⁸ D. R. Hamann, Phys. Rev. B **88**, 085117 (2013).

⁸⁹ X. Gonze, B. Amadon, G. Antonius, F. Arnardi, L. Baguet, J.-M. Beuken, J. Bieder, F. Bottin, J. Bouchet, E. Bousquet, N. Brouwer, F. Bruneval, G. Brunin, T. Cavignac, J.-B. Charraud, W. Chen, M. Côté, S. Cottetier, J. Denier, G. Geneste, P. Ghosez, M. Giantomassi, Y. Gillet, O. Gingras, D. R. Hamann, G. Hautier, X. He, N. Helbig, N. Holzwarth, Y. Jia, F. Jollet, W. Lafargue-Dit-Hauret, K. Lejaeghere, M. A. Marques, A. Martin, C. Martins, H. P. Miranda, F. Naccarato, K. Persson, G. Petretto, V. Planes, Y. Pouillon, S. Prokhorenko, F. Ricci, G.-M. Rignanese, A. H. Romero, M. M. Schmitt, M. Torrent, M. J. van Setten, B. Van Troeye, M. J. Verstraete, G. Zérah, and J. W. Zwanziger, Computer Physics Communications **248**, 107042 (2020).

⁹⁰ P. Giannozzi, O. Andreussi, T. Brumme, O. Bunau, M. B. Nardelli, M. Calandra, R. Car, C. Cavazzoni, D. Ceresoli, M. Cococcioni, N. Colonna, I. Carnimeo, A. D. Corso, S. de Gironcoli, P. Delugas, R. A. DiStasio, A. Ferretti, A. Floris, G. Fratesi, G. Fugallo, R. Gebauer, U. Gerstmann, F. Giustino, T. Gorni, J. Jia, M. Kawamura, H.-Y. Ko, A. Kokalj, E. Küçükbenli, M. Lazzeri, M. Marsili, N. Marzari, F. Mauri, N. L. Nguyen, H.-V. Nguyen, A. O. de-la Roza, L. Paulatto, S. Poncé, D. Rocca, R. Sabatini, B. Santra, M. Schlipf, A. P. Seitsonen, A. Smogunov, I. Timrov, T. Thonhauser, P. Umari, N. Vast, X. Wu, and S. Baroni, Journal of Physics: Condensed Matter **29**, 465901 (2017).